

Chandra Observation of the Starburst Galaxy NGC 2146

Tatsuya INUI¹, Hironori MATSUMOTO¹, Takeshi Go TSURU¹, Katsuji KOYAMA¹,
Satoki MATSUSHITA², Alison B. PECK³,
and

Andrea TARCHI^{4 5}

¹*Department of Physics, Graduate School of Science, Kyoto University, Sakyo-ku, Kyoto 606-8502, Japan;*
inuit@cr.scphys.kyoto-u.ac.jp

matsumoto@cr.scphys.kyoto-u.ac.jp

tsuru@cr.scphys.kyoto-u.ac.jp

koyama@cr.scphys.kyoto-u.ac.jp

²*Academia Sinica, Institute of Astronomy and Astrophysics, P.O.Box 23-141, Taipei 106, Taiwan, R.O.C.*
satoki@asiaa.sinica.edu.tw

³*Harvard-Smithsonian Center for Astrophysics, 60 Garden St., MS-78, Cambridge, MA 02138, U.S.A.*
apecck@cfa.harvard.edu

⁴*Istituto di Radioastronomia, CNR, Via Gobetti 101, 40129 Bologna, Italy*

⁵*Osservatorio Astronomico di Cagliari, Loc. Poggio dei Pini, Strada 54, 09012 Capoterra (CA), Italy*
atarchi@ira.cnr.it

(Received 2004 May 6; accepted 2004 October 29)

Abstract

We present six monitoring observations of the starburst galaxy NGC 2146 using the Chandra X-ray Observatory. We have detected 67 point sources in the $8'.7 \times 8'.7$ field of view of the ACIS-S detector. Six of these sources were Ultra-Luminous X-ray Sources, the brightest of which has a luminosity of 5×10^{39} ergs s^{-1} . One of the source, with a luminosity of $\sim 1 \times 10^{39}$ ergs s^{-1} , is coincident with the dynamical center location, as derived from the ^{12}CO rotation curve. We suggest that this source may be a low-luminosity active galactic nucleus. We have produced a table where the positions and main characteristics of the Chandra-detected sources are reported. The comparison between the positions of the X-ray sources and those of compact sources detected in NIR or radio does not indicate any definite counterpart. Taking profit of the relatively large number of sources detected, we have derived a $\log N - \log S$ relation and a luminosity function. The former shows a break at $\sim 10^{-15}$ ergs cm^{-2} s^{-1} , that we interpret as due to a detection limit. The latter has a slope above the break of 0.71, which is similar to those found in the other starburst galaxies. In addition, a diffuse X-ray emission has been detected in both, soft (0.5–2.0 keV) and hard (2.0–10.0 keV), energy bands. The spectra of the diffuse component has been fitted with a two (hard and soft) components. The hard power-law component, with a luminosity of $\sim 4 \times 10^{39}$ ergs s^{-1} , is likely originated by unresolved point sources, while the soft component is better described by a thermal plasma model with a temperature of 0.5 keV and high abundances for Mg and Si.

Key words: galaxies: starburst — galaxies: individual (NGC 2146) — galaxies: active — X-rays: galaxies

1. Introduction

ASCA observations have shown that X-ray spectra of starburst galaxies generally possess a hard component above 2 keV (Dahlem et al. 1998, Ptak et al. 1999). However, the origin of such a component is still unclear. In the prototype starburst galaxy M82, we found that most of the hard component is due to the most luminous X-ray source, M82 X-1, and that this object may belong to a new black holes class of objects, with $10^3 - 10^6 M_{\odot}$, named Intermediate-Mass Black Holes (IMBHs; Matsumoto et al. 2001). In another well-studied starburst galaxy, NGC 253, it is hot plasma with a temperature of 6 keV that accounts for the hard component (Pietsch et al. 2001).

Recently, we have studied 13 starburst galaxies previously observed with ASCA (Dahlem et al. 1998, Ptak et al. 1999). Among these we have found that NGC 2146 is the object with the high ratio of 2-10 keV X-ray to B-band luminosity ($\log L_X/L_B = 30.38$ ergs $s^{-1} L_{B,M_{\odot}}^{-1}$). In order to account for such a high ratio it is necessary for the presence of a large number (and maybe a different kind) of X-ray sources of emission than the usual X-ray binaries. This fact renders NGC 2146 the most interesting target in the sample to investigate the origin of the hard X-ray component.

NGC 2146 is a nearby ($D=11.6$ Mpc, $1' \sim 3.5$ kpc; Della Ceca et al. 1999) SB(s)ab, edge-on ($i \sim 63^\circ$) starburst galaxy. The optical size of the galaxy (D_{25} ellipse; at the limiting surface brightness of 25 B mag

arcsec⁻² after correction for Galactic extinction) is about $6'.0 \times 3'.4$ (de Vaucouleurs et al. 1991). The dynamical center of the galaxy lies toward a dense dust lane (Young et al. 1988). NGC 2146 has an outflow of hot gas along the minor axis driven by supernova explosions and stellar winds in the starburst region (Armus et al. 1995, Della Ceca et al. 1999, Greve et al. 2000). X-ray luminosities of NGC 2146 derived from the ASCA observation were $\sim 1.3 \times 10^{40}$, $\sim 1.8 \times 10^{40}$, and $\sim 3.1 \times 10^{40}$ ergs s⁻¹ in the soft (0.5–2.0 keV), hard (2.0–10.0 keV), and total (0.5–10.0 keV) energy bands, respectively (Della Ceca et al. 1999).

The unprecedented spatial resolution (0''.5) of Chandra makes it the most suitable instrument to determine whether the hard X-ray component of NGC 2146 is due to point sources such as IMBHs or to a hot diffuse plasma.

In this paper, we present the detailed catalog of point sources detected from the monitoring observations of NGC 2146 with Chandra and discuss their physical natures. Furthermore, we investigate the diffuse emission component and try to shed a light on the origin of the hard X-ray component. Errors and uncertainties in this paper refer to 90% confidence limits ($\Delta\chi^2=2.706$) unless otherwise stated.

2. Observations

NGC 2146 was observed six times through August to December 2002, with the Advanced CCD Imaging Spectrometer (ACIS; Garmire et al. 2003) on board the Chandra X-ray Observatory (CXO) (Weisskopf et al. 2002). The exposure time of each observation was about 10 ks, yielding a total observing time of 60 ks. Observations dates, exposure times and background levels are listed in Table 1. The nominal position of ACIS-S3 (a back-illuminated CCD on the spectroscopic array (ACIS-S) with good charge-transfer efficiency and good quantum efficiency below 0.5 keV) was selected coincident with the body of NGC 2146.

3. Analysis and Results

3.1. Imaging

For the following discussion it is worth to emphasize that, as explained in detail in the next section, there is no appreciable positional offsets among the observations performed at six different epochs. Hence, we were legitimate to combine the images. Using *dmimcalc* and *csmooth* program in the CIAO package version 2.3¹, we produced two adaptive smoothed maps of NGC 2146 in the two energy bands: 0.3–2.0 keV (Figures 1(a)) and 2.0–10.0 keV (Figures 1(b)), respectively. When compared to the optical image of the galaxy, the X-ray emission is found to be concentrated toward the nuclear region of NGC 2146. Shown in Figure 1(a) and Figure 1(b), the soft diffuse emission brows off from the galactic plane, while the hard diffuse radiation lies along the galactic plane.

¹ See <http://asc.harvard.edu/ciao/>

3.2. Point Sources

3.2.1. Source Detection

In order to establish the extent of the positional offsets between our multi-epoch Chandra maps, we run the *wavdetect* program in the CIAO package on the 0.3–10.0 keV image of each epoch.

Wavelet scales were from 1 to 16 pixels in multiples of $\sqrt{2}$. We found that among the six observations the positions of the two brightest sources are consistent within 0''.2, which is comparable to the Chandra positional accuracy of 0''.1².

Images at different epochs can be combined to increase signal-to-noise ratio and allow the detection of faint sources. Then, we run the *wavdetect* program on the combined images for three energy bands: total (0.3–10.0 keV), soft (0.3–2.0 keV) and hard (2.0–10.0 keV) energy bands, obtaining a detected source number of 62, 55 and 42, respectively. Since five sources are detected only in the soft (three sources) or hard (two sources) energy bands, we have a total number of 67 X-ray sources in the $8'.7 \times 8'.7$ ACIS-S field of view (FOV). 41 point sources are within the D_{25} ellipse at a 5σ level. We considered that these 41 sources belong to NGC 2146 and produce a $\log(N) - \log(S)$ distribution and a luminosity function for NGC 2146. Among these sources, about five sources are expected to be background sources which are within the D_{25} ellipse by chance (Giacconi et al. 2001).

In our analysis we have adopted the following assumption: the source regions' extent has been taken to be two times the standard deviation of the point spread function (PSF) at the detected positions. In most cases, as the background region, we used an ellipse twice as large as that of the source, excluding the source region. Instead at the galactic center the background region was selected close to the source because it was impossible to do otherwise due to the crowding of the field.

3.2.2. Timing Analysis

Light curves of the point sources have been created using the mean count rate of each observation and fitted with a constant count rate model. For five sources we obtained reduced χ^2 values larger than 11.05/5(dof), indicating, with a confidence level more than 95%, a significant variability with time. The light curves for these five variable sources are shown in Figure 2.

3.2.3. Spectral Analysis

We extracted the spectrum of each point source at each epoch and analyzed it with XSPEC version 11.0.1 in XANADU³. In order to use χ^2 statistics, we grouped the energy bins of the spectra so that each bin contains at least twenty counts. We fitted the spectra simultaneously with an absorbed power-law model. For each epoch, we used common values of the absorption column density N_{H} and the photon index Γ , while the normalization was left

² See <http://cxc.harvard.edu/cal/>

³ See <http://heasarc.gsfc.nasa.gov/docs/software/lheasoft/>

(a)

(b)

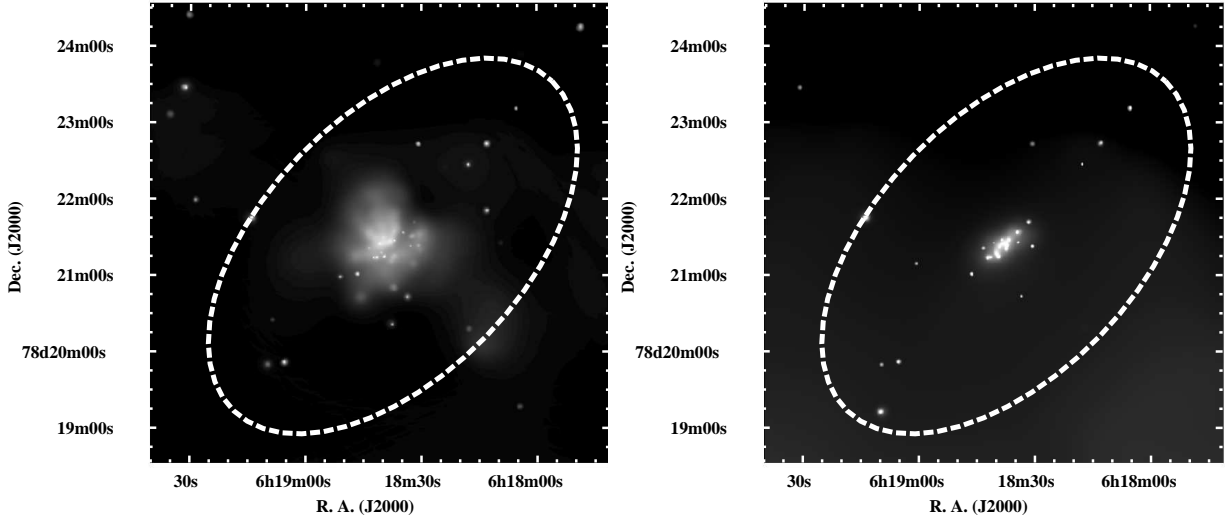


Fig. 1. Chandra ACIS-S $6'0 \times 6'0$ images of NGC 2146 in (a) the 0.3–2.0 keV and (b) the 2.0–10.0 keV energy bands. Each image is the combined image of the six observations and is adaptively smoothed. White dashed ellipses show D_{25} ellipses ($6'0 \times 3'4$) of NGC 2146.

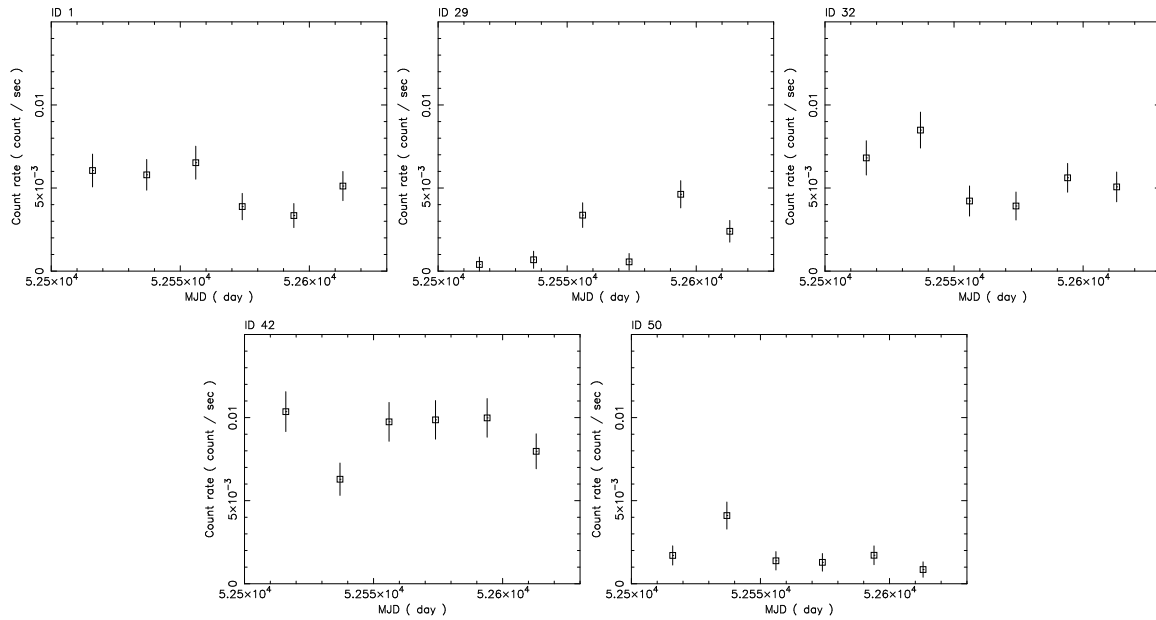


Fig. 2. Light curves of five time-variable sources in the 0.5–10.0 keV band. Error bars indicate 1σ .

Table 1. Log of the observations

Observation ID	Date (yyyy/mm/dd)	Exposure (s)	Background (counts s ⁻¹ arcmin ⁻²)
3131.....	2002/08/30	9,276	0.012
3132.....	2002/09/20	9,523	0.013
3133.....	2002/10/09	9,832	0.081
3134.....	2002/10/27	9,576	0.012
3135.....	2002/11/16	10,020	0.013
3136.....	2002/12/05	9,835	0.014
Total.....		58,062	

as a free parameter.

For bright sources having more than 180 total counts in the six observations, all parameters, N_{H} , Γ and normalizations, were free. For sources having less than 180 total counts, we fixed Γ to 2.0. For the faintest sources whose counts are less than 100 total counts, we combined the six spectra and fitted it with $\Gamma = 2.0$ and $N_{\text{H}} = 4.0 \times 10^{21} \text{ cm}^{-2}$, which is the best-fit N_{H} of the diffuse emission (see below). The observed flux and absorption corrected luminosity of the point sources in the 2.0–10.0 keV band and the 0.5–10.0 keV band are shown in the source list (Table 8). Seven sources (ID29,32,33,35,37,42,60) have luminosities of over $10^{39} \text{ ergs s}^{-1}$, and all except ID60 are within the D_{25} ellipse and considered to be Ultra-Luminous X-ray Sources (ULXs). ID60 is so remote from NGC 2146 that it should be a background AGN.

3.2.4. Diffuse Source

We extracted the spectra of the diffuse emission from a circular region at the center of NGC 2146 with a radius of 1/8 excluding the inner point sources. The background spectrum for each observation was extracted from a source-free rectangular region (about 5 arcmin² area) around the position (detX,detY)=(830,830) in detector coordinates. The background level of the third observation was 0.081 counts s⁻¹ arcmin⁻² and quite variable with an amplitude of 0.03 counts s⁻¹ arcmin⁻², while those of the other observations were ~ 0.01 counts s⁻¹ arcmin⁻² and stable during the observations. This effect can be ignored in the case of point sources while not in the case of the diffuse component due to the area where counts are accumulated. We therefore did not use the third observation for the analysis of the diffuse emission.

The derived spectra for the diffuse component are shown in Figure 3. We identified the strong spectral features as produced by Mg XI (1.33–1.35 keV) and Si XIII (1.84–1.87 keV). This suggests that the emission is originated by optically-thin thermal plasma. It was not possible to fit the spectra with an absorbed single-temperature plasma model with variable abundances ("vmekal" model; Mewe et al. 1985a, Mewe et al. 1985b, Liedahl et al. 1995).

Hence, we used instead a combination of a "vmekal" plus a power-law model with the same absorption column density for both models. The equivalent width of Fe K line (6.4 keV) was estimated to be ≤ 3 keV. An additional at-

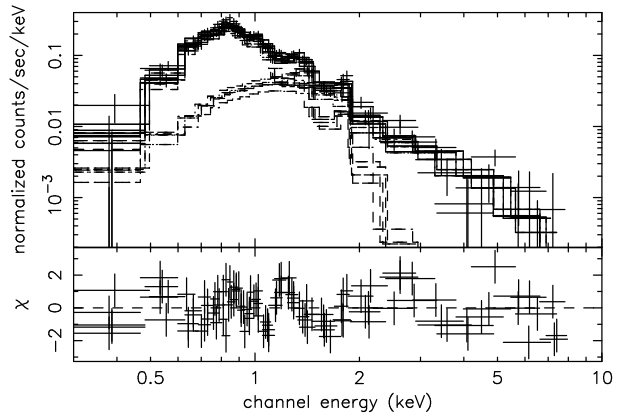


Fig. 3. Spectra of the diffuse emission (except the third observation) and the best-fit thin-thermal plasma plus power-law model. Features are seen between 1 and 2 keV, which are considered to come from Mg XI (1.33–1.35 keV) and Si XIII (1.84–1.87 keV) emission lines

tempt has been made to fit the spectra with the "vmekal" plus a thermal bremsstrahlung model. The derived parameters for both fits are summarized in Table 2.

Still some line-like residuals are found in Figure 3, however, we cannot improve χ^2 value to add another thermal component. The origin of this line component will be discussed in §4.3.2.

4. Discussion

4.1. Comparison with the ASCA results

In order to compare our Chandra data with the previous ASCA results (Della Ceca et al. 1999), we extract the entire NGC 2146 spectra from a circle at the center of the galaxy with a radius of 1/8 including the inner point sources. Since we spatially resolved point sources, we operate a simple spectral analysis to examine the overall flux variability.

We ignore those spectra with energies below 0.6 keV because in this range ASCA has no effective area. We use the same fitting model used by Della Ceca et al. (1999), an optically-thin thermal plasma model plus a power-law model. At first, all parameters except normalizations are fixed at the ASCA best-fit values, $N_{\text{H}} = 7 \times 10^{20} \text{ cm}^{-2}$, the plasma temperature of $kT = 0.82 \text{ keV}$, solar abundance and $\Gamma = 1.7$. Figure 4 shows the Chandra spectra

Table 2. Results of the spectral fits of the diffuse emission

Model	absorbed vmekal+power-law	absorbed vmekal+bremsstrahlung
N_{H} (10^{22}cm^{-2})	0.42 (0.31 – 0.58)	0.40 (0.27 – 0.66)
soft component		
kT_{soft} (keV)	0.30 (0.24 – 0.37)	0.31 (0.26 – 0.39)
Mg*	2.3 (1.8 – 3.0)	2.2 (1.7 – 3.1)
Si*	4.3 (2.0 – 7.2)	3.3 (1.2 – 7.5)
Fe*	0.80 (0.59 – 1.06)	0.73 (0.55 – 1.05)
$F_{0.5-2.0\text{keV}}^{\dagger}$ (10^{-13} ergs cm^{-2} s^{-1})	4.0	4.2
$L_{0.5-2.0\text{keV}}^{\dagger}$ (10^{40} ergs s^{-1})	3.6	3.2
hard component		
Γ/kT_{hard} (keV)	2.4 (2.1 – 2.7)	2.4 (1.8 – 3.5)
$F_{2.0-10.0\text{keV}}^{\ddagger}$ (10^{-13} ergs cm^{-2} s^{-1})	2.7	2.2
$L_{2.0-10.0\text{keV}}^{\ddagger}$ (10^{40} ergs s^{-1})	0.45	0.37
χ^2/dof	116/91	118/91

Note—Parentheses indicate the 90% confidence limit.

* Abundances are relative to the Anders et al. 1989 solar abundance.

\dagger Observed flux and absorption-corrected luminosity of the soft component in the 0.5-2.0 keV band.

\ddagger Observed flux and absorption-corrected luminosity of the hard component in the 2.0-10.0 keV band.

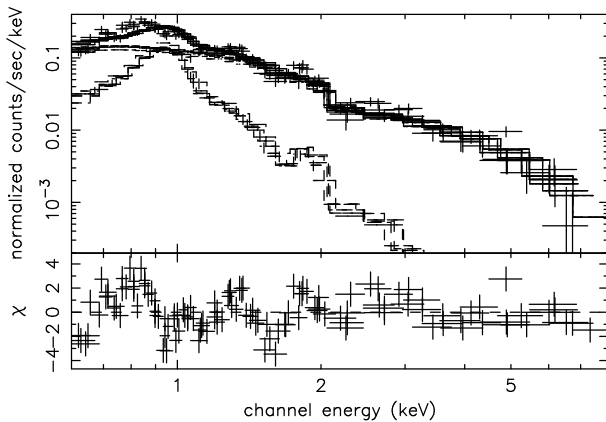


Fig. 4. Spectra of the entire NGC 2146 (except the third observation) and the ASCA two-component (thin-thermal plasma plus power-law) model. Large excess are found below 1 keV.

of NGC 2146 together with the ASCA model and residuals after the model is applied. It is noticeable that the model causes large residuals below 1 keV. We believe that this excess is real, since, below 1 keV, the Chandra ACIS-S has a better effective area than ASCA. Next, we fit them with all parameters free. The result is reported in Table 3. No significant difference in flux between two models is found while the residuals in the low energy band are improved. The power-law index Γ and the observed flux is comparable with the ASCA results. Therefore we conclude that the X-ray emission from the entire region of NGC 2146 shows no significant flux variability between our Chandra and the ASCA observations.

4.2. Point Sources

4.2.1. Search for an IMBH

The IMBH candidate M82 X-1 is a very hard source with a luminosity of over 10^{41} ergs s^{-1} , flux variation on

a time scale of $\sim 10^4$ s and off-center position (Matsumoto et al. 1999,2001). In our observations of NGC 2146, six ULXs are found and three of them (ID29,32,42) show time variations. The luminosity of the highest count-rate source ID42 is 2×10^{39} ergs s^{-1} but it is a rather soft (HR ~ -0.14) source. On the other hand, ID29 and ID32 are hard sources (HR ~ 0.55 and 0.44 , respectively) with luminosities of 3×10^{39} ergs s^{-1} and 4×10^{39} ergs s^{-1} , respectively. The light curve of ID29 (Figure 2) has two flare-like peaks and the count rate at the maximum peak is about three times larger than the average count rate. We find no point source whose luminosity is comparable to that of M82 X-1.

4.2.2. Identifications of the Chandra sources

In order to understand the nature of each point source, we searched for the NIR and radio counterparts using the 2MASS All-Sky Point Source Catalog(PSC)⁴ and the results of MERLIN+VLA observations (Tarchi et al. 2000) and found no positional coincidence between the detected X-ray point sources and those found in the NIR or radio band. The correlation method is explained in the following paragraph.

Figure 5 shows the distribution of NIR sources overlaid on the Chandra image. We picked up the closest NIR source from each X-ray source and did vice versa. Forty pairs were commonly selected in both the methods. Among the pairs, we found that three pairs have a distance of less than $0''.5$ between the X-ray and the NIR sources, and we found no pairs whose distance was less than $0''.2$. Next we checked the absolute positional offset of the ACIS-S coordinate. Using comparably nearby 10 pairs within $3''.0$, we shifted the ACIS-S frame to minimize the total distances of these pairs and searched pairs again. However, there were the same three pairs within $0''.5$, and were no pairs within $0''.2$. We then decided to

⁴ See <http://www.ipac.caltech.edu/2mass/>

Table 3. Comparison with the ASCA result

N_{H}	kT_{soft}	Abundance	Γ	$F_{0.5-2.0}$	$F_{2.0-10.0}$	χ^2/dof
(1)	(2)	(3)	(4)	(5)	(6)	(7)
0.07 (fixed)	0.82 (fixed)	1.0 (fixed)	1.7 (fixed)	5.9	9.9	260/110
0.15 (0.10–0.20)	0.59 (0.55–0.63)	0.63 (0.10–5.24)	1.7 (1.5–1.9)	5.8	9.8	174/106

Note—Parentheses indicate the 90% confidence limit. Col. (1): Absorption column density (10^{22} cm^{-2}). Col. (2): Plasma temperature (keV). Col. (3): Abundance (solar abundance). Col. (4): Photon index. Col. (5) and (6): Observed flux of the soft component in the 0.5–2.0 keV band and the 2.0–10.0 keV band ($10^{-13} \text{ ergs cm}^{-2} \text{ s}^{-1}$). Col. (7): χ^2 and degree of freedom.

use the original ACIS-S coordinate. The positional accuracy of Chandra is $0''.1^5$, while that of 2MASS sources is $\sim 80 \text{ mas}^6$. Therefore we concluded that there were no identifications with the NIR sources. We also searched for the radio counterparts using the results of the MERLIN and the VLA observations (Tarchi et al. 2000) in the same way as for the NIR identification. As the positional uncertainties of the MERLIN and the VLA are less than $0''.1^7$, we used the same criterion as 2MASS. We found no radio counterparts, either.

4.2.3. The galactic center source

We find the X-ray source ID33 with a luminosity of $1 \times 10^{39} \text{ ergs s}^{-1}$ at the dynamical center of NGC 2146 (R.A.= $06^{\text{h}}18^{\text{m}}37^{\text{s}}.4 \pm 0^{\text{s}}.4$, Dec.= $78^{\circ}21'23''.2 \pm 2''$) derived from a ^{12}CO rotation curve (Tarchi et al. 2000). Since the total counts of ID33 is only 113, we cannot make a complete spectral analysis. However, this source is a hard source (HR ~ 0.55) and the nearby source ID35 is also hard (HR ~ 0.58). As the dense dust lane (Young et al. 1988) is across these sources, it is natural to consider that they are strongly absorbed nuclear sources. The absorption column density under the assumption of a canonical AGN power-law spectral model ($\Gamma = 2.0$) is comparable with the value obtained by radio observations (Tarchi et al. 2004). ID33 may be a low-luminosity AGN (LLAGN). We note that the X-ray observations with Chandra have first exposed the nuclear region even under the heavy absorption.

4.2.4. The $\log N - \log S$ distribution and Luminosity Function

Figure 6 shows the $\log N - \log S$ distribution for NGC 2146, where S is the observed 2.0–10.0 keV flux. The $\log N - \log S$ has a sharp break at $\sim 2 \times 10^{-15} \text{ ergs cm}^{-2} \text{ s}^{-1}$, that might be due to an observational detection limit. In order to investigate this hypothesis, we have estimated an approximate possible value for such a limit. Within $0''.5$ from the center of NGC 2146, where the surface brightness of the diffuse emission is quite large, the typical counts due to the dif-

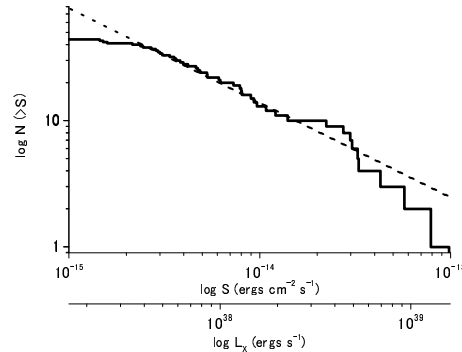


Fig. 6. $\log N - \log S$ distribution from NGC 2146. S is the observed 2.0–10.0 keV flux. The dashed line is the best-fit power-law model. The luminosity is calculated by $L_X = 4\pi D^2 \cdot S$, where D is the distance to NGC 2146. The absorption has a negligible effect in the high energy band.

fuse emission integrated for 60 ks within the typical PSF size ($0''.5$) is three counts. Therefore, if a source in this region has more than 12 counts, which corresponds to $\sim 1.3 \times 10^{-15} \text{ ergs cm}^{-2} \text{ s}^{-1}$, will be detected with high significance (more than 5σ). Since the flux is very close to the break point, we conclude that this break is probably due to the detection limit.

In the total band image, the flux of the faintest source in the central high diffuse emitting region is $\sim 2.0 \times 10^{-15} \text{ ergs cm}^{-2} \text{ s}^{-1}$. In the following discussion, we take this value as a conservative detection limit.

We also derive a luminosity function (LF) for NGC 2146 using the absorption-corrected 0.5–10.0 keV luminosities. The LF slope is 0.71. Hence, the LF for NGC 2146 is flatter than that of the normal spiral galaxies, while it is consistent with those of the other starburst galaxies (Kilgard et al. 2002). The fact indicates that the starburst galaxy NGC 2146, similarly to other starburst galaxies, has a large fraction of high X-ray luminosity sources.

4.2.5. Combined point source spectra

We combine the spectra of the point sources with fluxes larger than the detection limit and fitted them by a two-temperature bremsstrahlung model with all parameters free, since a power-law model, a bremsstrahlung or two-temperature combination models cannot describe the spectra. Spectra and the best-fit model are displayed in Figure 7. The best-fit parameters are listed in Table 4. The total observed flux of point sources in the 2.0–10 keV band is $7.8 \times 10^{-13} \text{ ergs cm}^{-2} \text{ s}^{-1}$. Since the

⁵ See <http://xc.harvard.edu/cal/Hrma/optaxis/platescale/geom.pu> for ACIS-S positional accuracy

⁶ See <http://www.ipac.caltech.edu/2mass/releases/allsky/doc/sec1.6b.html> for the 2MASS PSC Position Reconstruction

⁷ See http://www.merlin.ac.uk/user_guide/OnlineMUG/newch0-node104.html for the MERLIN Position accuracy, and <http://www.vla.nrao.edu/astro/guides/vlas/current/node20.html> for the VLA Positional Accuracy

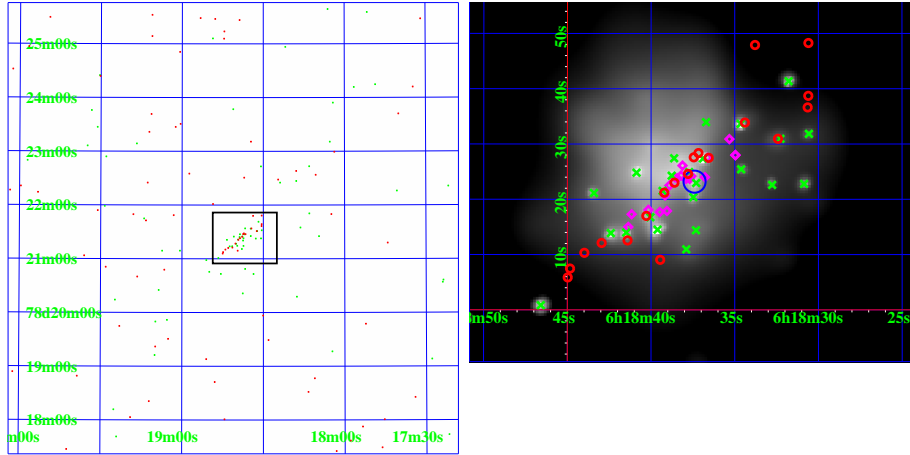


Fig. 5. Spatial distributions of the Chandra (green mark, cross), the 2MASS (red mark, circle) and the MERLIN and the VLA (magenta mark, diamond) sources. The magnified image around the galactic center (rectangle area in the left image) is shown in the right. A blue circle indicates the dynamical center.

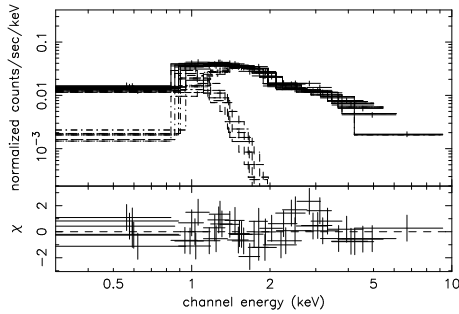


Fig. 7. Combined spectra of point sources with fluxes larger than 2×10^{-15} ergs cm^{-2} s^{-1} with the two-temperature bremsstrahlung model.

Table 4. Results of the spectral fits of the combined point sources

N_{H} (10^{21}cm^{-2})	9.9 (9.6 – 10.9)
kT_{brems1} (keV)	0.14 (0.12 – 0.16)
$F_{\text{brems1}}^{\dagger}$ (10^{-13} ergs cm^{-2} s^{-1})	0.43
kT_{brems2} (keV)	6.7 (5.8 – 9.0)
$F_{\text{brems2}}^{\dagger}$ (10^{-13} ergs cm^{-2} s^{-1})	9.0
χ^2/dof	39.4/35

Note—Parentheses indicate the 90% confidence limit.

\dagger Observed fluxes in the 0.5–10.0 keV band.

total flux coming from NGC 2146 in the same band is 9.8×10^{-13} ergs cm^{-2} s^{-1} , about 80% of the hard emission resides in the point sources, resolved by the high spatial resolution of Chandra. Table 5 shows the 2–10 keV emission ratios of detected point sources by Chandra to the total for six starburst galaxies. The hard emission of the starburst galaxies can be divided into two groups; point source dominant and diffuse source dominant.

Table 5. The 2–10 keV emission ratio of point sources to the total

point source dominant group	
NGC 2146	0.80
M82	0.70
the Antenna	0.81
diffuse source dominant group	
NGC 253	0.48
NGC 5253	0.38
NGC 3256	0.20

Reference to (Griffiths et al. 2000) for M82, (Fabbiano et al. 2001) for the Antenna, (Weaver et al. 2002) for NGC 253, (Summers et al. 2004) for MGC 5253, (Lira et al. 2002) for NGC 3256.

4.3. Diffuse Emission

4.3.1. Hard Component

The hard spectral component of the diffuse emission constitutes 20% of the hard (2.0–10.0 keV) emission produced in the whole galaxy, with a luminosity of $\sim 4 \times 10^{39}$ ergs s^{-1} . This luminosity is greater than the hard diffuse emission of M82 ($\sim 2 \times 10^{39}$ ergs s^{-1} ; Griffiths et al. 2000) and NGC 253 ($\sim 1 \times 10^{39}$ ergs s^{-1} ; Pietsch et al. 2001). Considered as a thermal plasma, the temperature is ~ 2.4 keV (Table 2). These features are quite similar to M82. To determine whether the origin of the hard component is a hot diffuse gas or a superposition of point sources unresolved even with Chandra, we estimate the contributions of the unresolved X-ray point sources.

At first, we try a spectral approach. We assume that the shape of the spectrum produced by a number of unresolved sources can be described through the same model used for the combined spectra of the resolved sources. Hence, we fit the diffuse emission in the same way described in §4.2.5. The model implying a collection of un-

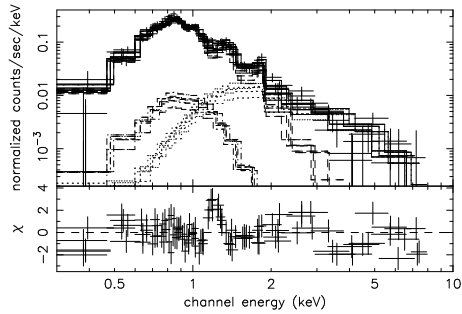


Fig. 8. Spectra of the diffuse source with the vmekal model plus the unresolved sources model.

resolved sources cannot fit the observed spectra, originating large residuals below 1 keV. Hence, we add the vmekal model and try again the fitting procedure and get an acceptable fit. The best-fit model are shown in Figure 8 and the best-fit parameters are listed in Table 6. The observed flux of the unresolved source component in the 2.0–10.0 keV band is 3.2×10^{-13} ergs cm^{-2} s^{-1} .

Next, we estimate the contributions of the unresolved X-ray sources by the $\log N - \log S$ distribution. The best-fit model function of the $\log N - \log S$ above 2×10^{-15} erg cm^{-2} s^{-1} can be described as

$$N(> S) = \int_S^\infty n(S) dS \\ = 49 \left(\frac{S}{2 \times 10^{-15} \text{ ergs cm}^{-2} \text{ s}^{-1}} \right)^{-0.75} \text{ sources,} \quad (1)$$

where $n(S)dS$ is the number of the sources with the flux S . By extrapolating the $\log N - \log S$ distribution below 2×10^{-15} erg cm^{-2} s^{-1} , we can calculate the total flux F of the sources having the flux between S_1 and S_2 by

$$F = \int_{S_1}^{S_2} S \cdot n(S) dS \\ = 2.9 \times 10^{-13} \left[\left(\frac{S}{2 \times 10^{-15} \text{ erg cm}^{-2} \text{ s}^{-1}} \right)^{0.25} \right]_{S_1}^{S_2} \text{ ergs cm}^{-2} \text{ s}^{-1}. \quad (2)$$

According to the equation (2), the flux of the unresolved sources between 0 and 2×10^{-15} ergs cm^{-2} s^{-1} is $F_{\text{unres}} = 2.9 \times 10^{-13}$ ergs cm^{-2} s^{-1} , which is very close to the flux derived by the spectral approach. Therefore we conclude that the hard emission of NGC 2146 is probably due to a superposition of unresolved point sources.

4.3.2. Soft Component

As shown in Figure 8, after having fitted the spectra clear residuals between 1.0 and 1.3 keV are still present. When we fitted this residual feature using a Gaussian function, we obtain a value for the feature's central position and width (FWHM) corresponding to $1.22_{-0.02}^{+0.01}$ keV and ≤ 96 eV, respectively. Since this feature is present at all epochs, we consider it as real. In this energy range, there are Ni emission lines. However the features cannot be accounted for by increasing the Ni abundance because Ni emission lines also exist at other energies. We tried to change the gain of ACIS with -22 eV, but the statis-

Table 7. Physical conditions of the soft X-ray-emitting gas

Parameter	Value
$\langle n_e \rangle$	$5.1 \times 10^{-3} f^{-1/2} \text{ cm}^{-3}$
p	$4.9 \times 10^{-12} f^{-1/2} \text{ dyne cm}^{-2}$
M_X	$1.3 \times 10^8 f^{1/2} M_\odot$
E_X	$2.3 \times 10^{56} f^{1/2} \text{ ergs}$

tics was not improved $\chi^2 = 120/91$ (dof). If we replace the soft component with a two-temperature thermal plasma model, statistics becomes $\chi^2 = 116/86$ (dof), but this is not an acceptable fit yet. This may indicate a neutral Mg emission line (1.25 keV). This problem will be resolved by the high energy resolution of Astro-E2 XRS⁸. We then estimated the physical parameters simply by using the parameters reported in Table 6.

The plasma temperature is determined to be $kT \sim 0.5$ keV. The plasma has the high abundances for Mg and Si. The emission integral ($\text{EI} = \int n_e^2 dV$) was calculated to be $8.0 \times 10^{62} \text{ cm}^{-3}$. We assumed that the total volume of NGC 2146 to be a sphere with a radius of $1/8 (= 6.3 \text{ kpc})$, and we parameterized the clumpiness of the plasma by a volume(V)-filling factor, f . From these values, we determined the plasma density [$n_e \sim (\text{EI}/Vf)^{1/2}$], the plasma pressure ($p \sim 2n_e kT$), the plasma mass ($M \sim n_e m_p V f$), and the thermal energy of the plasma ($E \sim 3n_e kTV f$). These physical parameters are listed in Table 7. The origin of the diffuse soft X-ray emission has been discussed and considered as an outflow gas along the minor axis of NGC 2146 (Armus et al. 1995).

5. Summary

We observed the starburst galaxy NGC 2146 with the ACIS-S on board Chandra in six different epochs, with a total exposure time of 60ks. We obtained the following results:

1. We detected a total of 67 point sources in the ACIS-S field of view and compiled an X-ray point source catalog for NGC 2146.
2. We did not detect any source as luminous as that found in the prototype starburst galaxy M82 (M82 X-1; luminosity $\sim 10^{41}$ ergs s^{-1}).
3. We found no positional coincidence, and hence, any association, between the detected X-ray point sources and those found in the NIR (2MASS All-Sky PSC) or radio (MERLIN+VLA observations) band.
4. We found a hard X-ray source coincident in position with the dynamical center of the galaxy. It has a luminosity of $\sim 1 \times 10^{39}$ ergs s^{-1} and it may represent a possible low-luminosity AGN (LLAGN) candidate.
5. We derived a $\log N - \log S$ distribution and a luminosity function (LF) for NGC 2146. The former shows a break that we demonstrated to be

⁸ See <http://www.isas.jaxa.jp/e/enterp/missions/astro-e2/>

Table 6. Results of the spectral fits of the diffuse emission with the unresolved sources component

thermal plasma (absorbed vmekal)	
N_{H} (10^{22}cm^{-2})	0.15 (0.12 – 0.20)
kT_{soft} (keV)	0.54 (0.50 – 0.57)
Mg*	1.9 (1.6 – 2.3)
Si*	2.0 (1.4 – 2.8)
Fe*	0.39 (0.34 – 0.45)
$F_{0.5-2.0\text{keV}}^{\dagger}$ (10^{-13} ergs cm^{-2} s^{-1})	4.9
$L_{0.5-2.0\text{keV}}^{\dagger}$ (10^{40} ergs s^{-1})	1.3
unresolved sources (absorbed two-temperature bremsstrahlung)	
N_{H} (10^{22}cm^{-2})	0.99 (fixed)
kT_{brems1} (keV)	0.14 (fixed)
kT_{brems2} (keV)	6.7 (fixed)
$F_{2.0-10.0\text{keV}}^{\ddagger}$ (10^{-13} ergs cm^{-2} s^{-1})	3.2
$L_{2.0-10.0\text{keV}}^{\ddagger}$ (10^{40} ergs s^{-1})	0.57
χ^2/dof	138/92

Note—Parentheses indicate the 90% confidence limit.

* Abundances are relative to the Anders et al. 1989 solar abundance.

† Observed flux and absorption-corrected luminosity of the soft component in the 0.5–2.0 keV band.

‡ Observed flux and absorption-corrected luminosity of the hard component in the 2.0–10.0 keV band.

likely caused by detection limit. The slope of LF is 0.71, consistent with that of other starburst galaxies. This represents an indication that NGC 2146, as well as other starbursts, hosts a larger fraction of luminous sources than normal galaxies.

6. We have mapped diffuse emission in both the soft (0.5–2.0 keV) and hard (2.0–10.0 keV) energy bands. The spectra were fitted using a two-component model: a soft and a hard one.
7. The point sources produce most of the hard emission in NGC 2146 and even the hard component of the diffuse emission, with a luminosity of $\sim 4 \times 10^{39}$ ergs s^{-1} , is probably accounted for by unresolved point sources.
8. The diffuse emission soft component is described by a thermal plasma model with a temperature of $kT \sim 0.5$ keV with high abundances for Mg and Si. We also determined the physical parameters of the soft X-ray-emitting gas.

Acknowledgement

We would like to thank the anonymous referee for a considered, helpful and prompt report. This work is supported by the Grant-in-Aid for the 21st Century COE "Center for Diversity and Universality in Physics" from the Ministry of Education, Culture, Sports, Science and Technology (MEXT) of Japan. This work was supported in part by a grant-in-aid for scientific research 15740119 from the Japan Society for the promotion of Science (JSPS). Support for this work was provided by the National Aeronautics and Space Administration through Chandra Award Number GO2-3153X issued by the Chandra X-ray Observatory Center, which is operated by the Smithsonian Astrophysical Observatory for and on behalf of the National Aeronautics and Space Administration under contract NAS8-39073.

References

- Anders, E., & Grevesse, N. 1989, *Geochim. Cosmochim. Acta*, 53, 197
- Armus, L., Heckman, T. M., Weaver, K. A., & Lehnert, M. D. 1995, *ApJ*, 445, 666
- Dahlem, M., Weaver, K. A., & Heckman, T. M. 1997, *ApJS*, 18, 401
- Della Ceca, R., Griffiths, R. E., Heckman, T. M., Lehnert, M. D., & Weaver, K. A. 1999, *ApJ*, 514, 772
- de Vaucouleurs, G., de Vaucouleurs, A., Corwin, H., Buta, R., Paturel, R., & Fouque, P. 1991, *Third Reference Catalog of Bright Galaxies* (Austin: Univ. Texas Press)
- Fabbiano, G., Zezas, A., & Murray, S. S. 2000, *ApJ*, 554, 1035
- Garmire, G. P., Bautz, M. W., Ford, P. G., Nousek, J. A., & Ricker, G. R., Jr. 2003, *Proc. SPIE*, 4851, 28
- Giacconi, R., Rosati, P., Tozzi, P., Nonino, M., Gasinger, G., Norman, C., Bergeron, J., Borgani, S., Gilli, R., Gilmozzi, R., & Zheng, W. 2001, *ApJ*, 551, 624
- Greve, A., Neininger, N., Tarchi, A., & Sievers, A. 2000, *A&AS*, 364, 409
- Griffiths, R. E., Ptak, A., Feigelson, E. D., Garmine, G., Townsley, L., Brandt, W. N., Sambruna, R., & Bregman, J. N. 2000, *Science*, 290, 1325
- Kilgard, R. E., Kaaret, P., Krauss, M. I., Prestwich, A. H., Raley, M. T., & Zezas, A. 2002, *ApJ*, 573, 138
- Liedahl, D. A., Osterheld, A. L., & Goldstein, W. H. 1995, *ApJL*, 438, L115
- Lira, P., Ward, M., Zeza, A., Alonso-Herrero, A., & Ueno, S. 2002, *MNRAS*, 330, 259
- Matsumoto, H., & Tsuru, T. G. 1999, *PASJ*, 51, 321
- Matsumoto, H., Tsuru, T. G., Koyama, K., Awaki, H., Canizares, C. R., Kawai, N., Matsushita, S., & Kawabe, R. 2001, *ApJL*, 547, L25
- Matsushita, S., Kawabe, R., Matsumoto, H., Tsuru, T. G., Kohno, K., Morita, K. I., Okumura, S. K., & Vila-Vilar, B. 2001, *ApJL*, 545, L107
- Mewe, R., Gronenschild, E. H. B. M., & van den Oord, G. H. J. 1985b, *A&AS*, 62, 197

- Mewe, R., Lemen, J. R., & van den Oord, G. H. J. 1985b, *A&AS*, 65, 511
- Pietsch, W., Roberts, T. P., Sako, M., Freyberg, M. J., Read, A. M., Borozdin, K. N., Branduardi-Raymont, G., Cappi, M., Ehle, M., Ferrando, P., Kahn, S. M., Ponman, T. J., Ptak, A., Shirey, R. E., & Ward, M. 2001, *A&AS*, 365, L174
- Ptak, A., Serlemitsos, P., Yaqoob, T., & Mushotzky, R. 1999, *ApJS*, 120, 179
- Summers, L. K., Stevens, I. R., Strickland, D. K., & Heckman, T. M. 2004, *MNRAS*, 351, 1
- Tarchi, A., Neininger, N., Greve, A., Klein, U., Garrington, S. T., Muxlow, T. W. B., Pedlar, A., & Glendenning, B. E. 2000, *A&A*, 358, 95
- Tarchi, A., Greve, A., Peck, A. B., Neininger, N., Wills, K. A., Pedlar, A., & Klein, U. 2004, *MNRAS*, 351, 339
- Weaver, K. A., Heckman, T. M., Strickland, D. K., & Dahlem, M. 2002, *ApJL*, 576, L19
- Weisskopf, M. C., Brinkman, B., Canizares, C., Garmire, G., Murray, S., & Van Speybreck, L. P. 2002, *PASP*, 114, 1
- Young, J. S., Claussen, M. J., Kleinmann, S. G., Rubin, V. C., & Scoville, N. 1988, *ApJL*, 331, 81

Table 8. Main Chandra Point Source Catalog

ID	R.A. (J2000)	Dec. (J2000)	Net Counts (1)	Significance (2)	Time Variability (3)	Hardness Ratio (4)	N_H (5)	Γ (6)	$F_{X,2-10}$ (7)	$F_{X,0.5-10}$ (8)	$\log L_{X,2-10}$ (9)	$\log L_{X,0.5-10}$ (10)
1	06 ^h 17 ^m 21 ^s .69	+78°22′21″.3	339.6 ± 18.8	67.6	0.95	-0.43 (-0.49 - -0.38)	0.10 (... - 0.36)	1.62 (1.17 - 2.76)	3.30	4.56	38.73	38.90
2	06 ^h 17 ^m 21 ^s .73	+78°17′43″.7	8.9 ± 3.3	3.3	0.05	-0.66 (... - -0.42)	<i>b</i>	<i>a</i>	0.08	0.10	37.11	37.38
3	06 ^h 17 ^m 23 ^s .64	+78°20′36″.3	36.4 ± 6.3	11.8	0.42	-0.83 (-0.94 - -0.72)	<i>b</i>	<i>a</i>	0.31	0.42	37.71	37.98
4	06 ^h 17 ^m 23 ^s .88	+78°20′33″.9	61.2 ± 8.1	18.3	0.74	-0.75 (-0.85 - -0.65)	<i>b</i>	<i>a</i>	0.47	0.65	37.90	38.17
5	06 ^h 17 ^m 40 ^s .68	+78°22′16″.0	40.3 ± 6.7	12.0	0.28	-0.62 (-0.77 - -0.50)	<i>b</i>	<i>a</i>	0.38	0.52	37.81	38.08
6	06 ^h 17 ^m 48 ^s .59	+78°24′14″.7	65.2 ± 8.3	20.9	0.75	-0.48 (-0.61 - -0.37)	<i>b</i>	<i>a</i>	0.77	1.05	38.11	38.38
7	06 ^h 17 ^m 51 ^s .58	+78°25′35″.4	24.3 ± 5.3	7.8	0.02	0.00 (-0.26 - 0.19)	<i>b</i>	<i>a</i>	0.29	0.39	37.68	37.95
8	06 ^h 17 ^m 56 ^s .48	+78°24′11″.7	6.5 ± 2.6	3.1	0.00	-0.48 (... - -0.16)	<i>b</i>	<i>a</i>	0.09	0.13	37.19	37.46
9	06 ^h 18 ^m 04 ^s .24	+78°23′54″.3	8.5 ± 3.0	4.1	0.03	-0.18 (-0.89 - 0.18)	<i>b</i>	<i>a</i>	0.09	0.12	37.18	37.45
10	06 ^h 18 ^m 04 ^s .60	+78°19′16″.6	18.6 ± 4.8	5.7	0.08	-0.27 (-0.54 - -0.08)	<i>b</i>	<i>a</i>	0.20	0.27	37.52	37.79
11	06 ^h 18 ^m 05 ^s .40	+78°23′10″.7	58.3 ± 7.8	20.4	0.04	0.17 (0.02 - 0.30)	<i>b</i>	<i>a</i>	0.99	1.35	38.22	38.49
12	06 ^h 18 ^m 06 ^s .13	+78°25′38″.8	11.2 ± 3.6	4.3	0.02	0.36 (0.00 - 0.60)	<i>b</i>	<i>a</i>	0.18	0.25	37.52	37.79
13	06 ^h 18 ^m 09 ^s .46	+78°21′25″.3	15.1 ± 4.5	4.5	0.15	-0.40 (-0.71 - -0.19)	<i>b</i>	<i>a</i>	0.19	0.26	37.50	37.77
14	06 ^h 18 ^m 13 ^s .01	+78°21′50″.7	40.4 ± 6.7	12.2	0.14	-0.74 (-0.86 - -0.65)	<i>b</i>	<i>a</i>	0.46	0.63	37.89	38.16
15	06 ^h 18 ^m 13 ^s .06	+78°22′43″.3	109.1 ± 10.8	18.9	0.80	-0.50 (-0.60 - -0.42)	<i>b</i>	<i>a</i>	1.08	1.47	38.26	38.53
16	06 ^h 18 ^m 16 ^s .30	+78°21′34″.9	10.1 ± 3.7	3.2	0.12	0.03 (-0.36 - 0.28)	<i>b</i>	<i>a</i>	0.12	0.16	37.30	37.57
17	06 ^h 18 ^m 17 ^s .63	+78°20′17″.7	15.3 ± 4.2	5.4	0.42	-0.58 (-0.88 - -0.37)	<i>b</i>	<i>a</i>	0.15	0.21	37.40	37.67
18	06 ^h 18 ^m 17 ^s .84	+78°22′26″.9	76.4 ± 9.1	21.7	0.93	-0.36 (-0.48 - -0.26)	<i>b</i>	<i>a</i>	0.81	1.10	38.13	38.40
19	06 ^h 18 ^m 21 ^s .83	+78°24′56″.6	7.2 ± 2.8	3.2	0.04	-0.76 (... - -0.51)	<i>b</i>	<i>a</i>	0.15	0.20	37.39	37.66
20	06 ^h 18 ^m 23 ^s .81	+78°22′25″.0	17.2 ± 4.5	5.9	0.04	-0.16 (-0.49 - 0.06)	<i>b</i>	<i>a</i>	0.16	0.22	37.43	37.70
21	06 ^h 18 ^m 30 ^s .57	+78°21′31″.8	39.2 ± 7.5	7.6	0.37	-0.28 (-0.47 - -0.14)	<i>b</i>	<i>a</i>	0.42	0.57	37.85	38.12
22	06 ^h 18 ^m 30 ^s .86	+78°21′22″.8	56.6 ± 9.0	9.4	0.44	-0.06 (-0.22 - 0.07)	<i>b</i>	<i>a</i>	0.73	0.99	38.09	38.36
23	06 ^h 18 ^m 30 ^s .86	+78°22′43″.2	56.6 ± 7.9	15.4	0.81	-0.56 (-0.69 - -0.45)	<i>b</i>	<i>a</i>	0.53	0.72	37.95	38.22
24	06 ^h 18 ^m 31 ^s .78	+78°21′41″.4	67.9 ± 9.1	13.6	0.21	0.58 (0.48 - 0.67)	<i>b</i>	<i>a</i>	0.62	0.85	38.02	38.29
25	06 ^h 18 ^m 32 ^s .27	+78°21′31″.0	28.2 ± 6.6	5.6	0.03	-0.68 (-0.87 - -0.52)	<i>b</i>	<i>a</i>	0.36	0.49	37.78	38.05
26	06 ^h 18 ^m 32 ^s .77	+78°21′22″.6	32.4 ± 7.2	5.9	0.33	-0.49 (-0.68 - -0.34)	<i>b</i>	<i>a</i>	0.37	0.50	37.79	38.06
27	06 ^h 18 ^m 33 ^s .61	+78°20′43″.1	50.5 ± 7.5	14.4	0.60	-0.16 (-0.32 - -0.03)	<i>b</i>	<i>a</i>	0.49	0.66	37.91	38.18
28	06 ^h 18 ^m 34 ^s .62	+78°21′25″.4	25.5 ± 6.3	5.2	0.28	0.53 (0.36 - 0.66)	<i>b</i>	<i>a</i>	0.29	0.39	37.68	37.95
29	06 ^h 18 ^m 34 ^s .65	+78°21′33″.7	124.0 ± 12.3	20.0	1.00	0.57 (0.49 - 0.64)	2.30 (1.67 - 3.06)	<i>a</i>	3.26	3.49	38.81	39.08
30	06 ^h 18 ^m 36 ^s .71	+78°21′34″.0	32.5 ± 7.1	6.2	0.01	-1.27 ^c	<i>b</i>	<i>a</i>	0.53	0.72	37.95	38.22
31	06 ^h 18 ^m 36 ^s .71	+78°20′48″.7	23.9 ± 5.6	6.3	0.27	-0.44 (-0.68 - -0.26)	<i>b</i>	<i>a</i>	0.25	0.33	37.61	37.88
32	06 ^h 18 ^m 36 ^s .90	+78°21′27″.4	349.9 ± 10.3	38.9	0.99	0.44 (0.39 - 0.48)	2.95 (1.22 - 5.73)	2.23 (1.21 - 3.53)	9.82	10.42	39.32	39.66
33	06 ^h 18 ^m 37 ^s .30	+78°21′23″.0	112.9 ± 12.4	15.3	0.33	0.55 (0.47 - 0.62)	2.04 (1.33 - 3.01)	<i>a</i>	3.05	3.31	38.77	39.04
34	06 ^h 18 ^m 37 ^s .32	+78°21′14″.4	16.8 ± 5.2	3.9	0.03	-2.60 ^c	<i>b</i>	<i>a</i>	0.21	0.28	37.54	37.81
35	06 ^h 18 ^m 37 ^s .47	+78°21′20″.4	88.0 ± 11.6	11.1	0.68	0.58 (0.50 - 0.66)	2.35 (1.64 - 3.39)	<i>a</i>	2.98	3.18	38.77	39.04
36	06 ^h 18 ^m 37 ^s .57	+78°20′21″.4	31.1 ± 5.9	9.8	0.17	-0.36 (-0.56 - -0.20)	<i>b</i>	<i>a</i>	0.29	0.40	37.69	37.93
37	06 ^h 18 ^m 37 ^s .72	+78°21′24″.9	229.3 ± 16.8	27.4	0.22	0.18 (0.11 - 0.24)	1.12 (... - ...)	1.94 (... - ...)	4.29	4.96	38.89	39.14
38	06 ^h 18 ^m 37 ^s .90	+78°21′11″.0	32.2 ± 7.1	6.1	0.02	-0.59 (-0.78 - -0.45)	<i>b</i>	<i>a</i>	0.40	0.54	37.82	38.09
39	06 ^h 18 ^m 38 ^s .62	+78°21′27″.4	117.4 ± 12.5	16.1	0.40	-0.21 (-0.31 - -0.12)	0.25 (0.06 - 0.68)	<i>a</i>	0.97	1.42	38.20	38.47
40	06 ^h 18 ^m 38 ^s .77	+78°21′24″.3	214.3 ± 17.1	21.5	0.38	-0.21 (-0.29 - -0.15)	0.31 (... - 0.77)	1.86 (1.01 - 2.94)	2.23	3.01	38.57	38.80
41	06 ^h 18 ^m 39 ^s .31	+78°21′21″.5	46.7 ± 7.5	10.8	0.66	0.62 (0.51 - 0.72)	<i>b</i>	<i>a</i>	0.90	1.23	38.18	38.45
42	06 ^h 18 ^m 39 ^s .61	+78°21′14″.5	568.0 ± 24.9	68.7	0.96	-0.14 (-0.19 - -0.10)	1.08 (0.71 - 1.52)	2.33 (2.06 - 2.89)	7.88	9.83	39.16	39.54
43	06 ^h 18 ^m 40 ^s .04	+78°21′16″.8	77.4 ± 10.2	12.2	0.27	0.63 (0.53 - 0.72)	<i>b</i>	<i>a</i>	0.61	0.83	38.01	38.28
44	06 ^h 18 ^m 40 ^s .87	+78°21′24″.8	273.3 ± 18.7	28.2	0.43	-0.71 (-0.77 - -0.66)	0.26 (0.14 - 0.44)	<i>a</i>	1.40	2.03	38.36	38.63
45	06 ^h 18 ^m 41 ^s .10	+78°23′47″.0	8.3 ± 3.0	3.8	0.01	0.10 (-0.43 - 0.40)	<i>b</i>	<i>a</i>	0.14	0.20	37.39	37.66
46	06 ^h 18 ^m 41 ^s .49	+78°21′14″.0	132.6 ± 13.4	16.7	0.37	-0.39 (-0.47 - -0.31)	0.26 (0.07 - 0.47)	<i>a</i>	1.21	1.77	38.30	38.57
47	06 ^h 18 ^m 42 ^s .40	+78°21′13″.9	149.2 ± 13.8	20.0	0.65	0.14 (0.05 - 0.22)	1.19 (0.80 - 1.69)	<i>a</i>	2.74	3.17	38.69	38.96
48	06 ^h 18 ^m 43 ^s .41	+78°21′21″.1	66.3 ± 10.0	9.8	0.02	-0.29 (-0.43 - -0.17)	<i>b</i>	<i>a</i>	0.80	1.09	38.13	38.40
49	06 ^h 18 ^m 45 ^s .64	+78°20′43″.1	22.4 ± 5.2	6.8	0.38	-0.09 (-0.34 - 0.09)	<i>b</i>	<i>a</i>	0.27	0.37	37.66	37.93
50	06 ^h 18 ^m 46 ^s .58	+78°21′00″.8	112.1 ± 11.3	22.6	0.97	-0.50 (-0.59 - -0.42)	0.31 (0.17 - 0.49)	<i>a</i>	0.93	1.32	38.19	38.46
51	06 ^h 18 ^m 48 ^s .65	+78°25′06″.1	257.6 ± 16.3	66.8	0.93	-0.47 (-0.53 - -0.41)	0.34 (0.11 - 0.52)	2.63 (1.97 - 3.71)	1.33	2.48	38.35	38.85
52	06 ^h 18 ^m 49 ^s .92	+78°20′45″.4	15.3 ± 4.4	4.9	0.00	-0.14 (-0.43 - 0.07)	<i>b</i>	<i>a</i>	0.18	0.25	37.49	37.76
53	06 ^h 18 ^m 51 ^s .01	+78°20′58″.6	26.8 ± 5.7	7.8	0.13	-0.93 (... - -0.87)	<i>b</i>	<i>a</i>	0.21	0.29	37.56	37.83
54	06 ^h 19 ^m 00 ^s .74	+78°21′09″.0	22.1 ± 5.2	6.5	0.12	0.66 (0.47 - 0.81)	<i>b</i>	<i>a</i>	0.24	0.32	37.60	37.87
55	06 ^h 19 ^m 05 ^s .48	+78°19′51″.7	125.0 ± 11.4	34.6	0.47	-0.60 (-0.68 - -0.52)	0.15 (0.05 - 0.27)	<i>a</i>	0.79	1.24	38.11	38.38
56	06 ^h 19 ^m 07 ^s .32	+78°21′09″.0	8.3 ± 3.2	3.2	0.07	-0.62 (-0.95 - -0.39)	<i>b</i>	<i>a</i>	0.05	0.07	36.95	37.22
57	06 ^h 19 ^m 08 ^s .54	+78°20′25″.1	15.9 ± 4.4	5.4	0.13	-0.28 (-0.60 - -0.06)	<i>b</i>	<i>a</i>	0.14	0.20	37.39	37.66
58	06 ^h 19 ^m 09 ^s .74	+78°19′49″.9	31.6 ± 6.0	9.7	0.01	-0.06 (-0.27 - 0.10)	<i>b</i>	<i>a</i>	0.34	0.46	37.75	38.02
59	06 ^h 19 ^m 10 ^s .00	+78°19′12″.5	38.2 ± 6.5	12.1	0.01	0.95 (0.90 - ...)	<i>b</i>	<i>a</i>	0.15	0.21	37.40	37.67
60	06 ^h 19 ^m 13 ^s .98	+78°21′45″.0	391.4 ± 20.0	92.8	0.48	0.10 (0.05 - 0.15)	2.40 (1.17 - 6.54)	2.53 (1.19 - 6.06)	5.73	6.84	39.11	39.26
61	06 ^h 19 ^m 16 ^s .72	+78°23′08″.7	12.0 ± 3.7	4.5	0.04	-0.36 (-0.74 - -0.12)	<i>b</i>	<i>a</i>	0.11	0.16	37.28	37.55
62	06 ^h 19 ^m 24 ^s .04	+78°17′41″.4	53.4 ± 8.2	11.2	0.79	-0.07 (-0.22 - 0.06)	<i>b</i>	<i>a</i>	0.59	0.81	38.00	38.27
63	06 ^h 19 ^m 28 ^s .00	+78°22′54″.1	7.0 ± 2.8	3.0	0.00	1.00	<i>b</i>	<i>a</i>	0.01	0.02	36.29	36.56
64	06 ^h 19 ^m 28 ^s .52	+78°21′58″.9	28.6 ± 5.7	9.4	0.10	-0.29 (-0.51 - -0.12)	<i>b</i>	<i>a</i>	0.30	0.41	37.71	37.98
65	06 ^h 19 ^m 30 ^s .46	+78°24′24″.8	9.9 ± 3.3	4.2	0.00	-1.00	<i>b</i>	<i>a</i>	0.06	0.08	37.01	37.28
66	06 ^h 19 ^m 31 ^s .23	+78°23′27″.0	109.7 ± 10.8	30.1	0.42	-0.66 (-0.74 - -0.59)	<i>b</i>	<i>a</i>	1.13	1.55	38.28	38.55
67	06 ^h 19 ^m 34 ^s .92	+78°23′06″.3	22.1 ± 5.0	7.6	0.06	0.03 (-0.26 - 0.24)	<i>b</i>	<i>a</i>	0.23	0.31	37.59	37.86

Notes—Parentheses indicate the 90% confidence limit. No value in a parenthesis means that error is not constrained. Col.(1): Photon counts and errors with background subtracted. Col.(2): Source significance (σ). Col.(3): Time variability given with the χ^2 test. Col.(4): Hardness Ratio (HR) derived by the equation $(h - s)/(h + s)$, h is hard band counts (2.0–10.0 keV) and s is soft band counts (0.5–2.0 keV). Col.(5): Absorption column density (10^{22} cm^{-2}). Col.(6): Photon index. Col.(7) & (8): Observational flux in the 2.0–10.0 keV and the 0.5–10.0 keV band ($10^{-14} \text{ ergs cm}^{-2} \text{ s}^{-1}$). Col.(9) & (10): Absorption-corrected luminosity in the 2.0–10.0 keV and the 0.5–10.0 keV band. (ergs s^{-1})

^a Photon index fixed at 2.0 due to low number of counts (< 180 counts).

^b Absorption column density fixed at 0.4 (10^{22} cm^{-2}), the best-fit value of the diffuse emission (< 120 counts).

^c Since a background-subtracted hard band counts drop into minus, HR shows less than -1.